X-Band Polarimetric Observations of Cross Coupling in the Ice Phase of Convective Storms in Taiwan

J. C. HUBBERT, S. M. ELLIS, AND W.-Y. CHANG

National Center for Atmospheric Research, Boulder, Colorado

Y.-C. LIOU

Department of Atmospheric Sciences, National Central University, Jhongli City, Taiwan

(Manuscript received 26 November 2013, in final form 6 March 2014)

ABSTRACT

In this paper, experimental X-band polarimetric radar data from simultaneous transmission of horizontal (H) and vertical (V) polarizations (SHV) are shown, modeled, and microphysically interpreted. Both range–height indicator data and vertical-pointing X-band data from the Taiwan Experimental Atmospheric Mobile-Radar (TEAM-R) are presented. Some of the given X-band data are biased, which is very likely caused by cross coupling of the H and V transmitted waves as a result of aligned, canted ice crystals. Modeled SHV data are used to explain the observed polarimetric signatures. Coincident data from the National Center for Atmospheric Research S-band polarimetric radar (S-Pol) are presented to augment and support the X-band polarimetric observations and interpretations. The polarimetric S-Pol data are obtained via fast-alternating transmission of horizontal and vertical polarizations (FHV), and thus the S-band data are not contaminated by the cross coupling (except the linear depolarization ratio LDR) observed in the X-band data. The radar data reveal that there are regions in the ice phase where electric fields are apparently aligning ice crystals near vertically and thus causing negative specific differential phase K_{dp}. The vertical-pointing data also indicate the presence of preferentially aligned ice crystals that cause differential reflectivity Z_{dr} and differential phase ϕ_{dp} to be strong functions of azimuth angle.

1. Introduction

With the rapid proliferation of X-band weather radars that use simultaneous transmission of horizontal (H) and vertical (V) polarizations [termed SHV mode here, but also known as simultaneous transmit and reception mode (STAR)] to achieve dual polarization, it is of increasing interest to investigate and interpret the well-known cross-coupling biases that appear in the ice phase of storms. These dual-polarization weather radars are becoming common because of their ability to offer a better description of precipitation when compared with single-polarization radars. Seliga and Bringi (1976) were the first to suggest the use of SHV radar data. Doviak et al. (2000) more recently evaluated SHV mode for use in the National Weather Service Next-Generation Weather Radar (NEXRAD) program. In contrast, the National Center for Atmospheric Research (NCAR) S-band dual-polarization Doppler radar (S-Pol) typically uses fast-alternating H and V transmit pulses (termed FHV here) to achieve dual-polarization measurements. S-Pol can operate in SHV mode as well.

A well-known consequence of the SHV technique is that cross coupling of the H and V transmit waves can occur, which has been shown to bias polarimetric measurements, especially differential reflectivity Z_{dr} (Ryzhkov and Zrnić 2007; Wang and Chandrasekar 2006; Hubbert et al. 2010a,b). Cross coupling occurs when part of the H-polarized (V polarized) component of the electric field is transformed to V polarization (H polarization), thereby causing bias in the SHV polarimetric variables. The two primary mechanisms that cause cross coupling are 1) antenna polarization errors (McCormick and Hendry 1975; Hubbert et al. 2010a) and 2) forward scatter through a medium of precipitation particles that have a significant

Corresponding author address: J. C. Hubbert, National Center for Atmospheric Research, 3450 Mitchell Lane, Boulder, CO 80301.
E-mail: hubbert@ucar.edu

DOI: 10.1175/JAMC-D-13-0360.1

nonzero mean canting angle, relative to the horizontal direction in the radar plane of polarization. One such medium is ice crystals that are canted because of an electric field (Hendry and Antar 1982; Caylor and Chandrasekar 1996; Metcalf 1995; Krehbiel et al. 1996). Such aligned, canted ice particles bias not only SHV Z_{dr} but also linear depolarization ratio LDR in FHV mode (Ryzhkov and Zrnić 2007). Biases caused by antenna polarization errors are negligible in comparison with the biases caused by the canted ice crystals and are not considered in this paper.

Both Ryzhkov and Zrnić (2007) and Hubbert et al. (2010a) have modeled biases caused by cross coupling from propagation media with a nonzero mean canting angle. In this paper, the modeled radar data presented in Hubbert et al. (2010a) are expanded: the effects of a range of differential transmit phases coupled with various mean canting angles of scatterers in the propagation medium are given. Such modeling is important for interpreting the experimentally observed effects of cross coupling on SHV Z_{dr} (Z_{dr}^{shv}) and SHV differential phase ϕ_{dp} (ϕ_{dp}^{shv}) for various values of the transmit differential phase, which is the phase difference between the H and V transmitted waves as the waves emerge from the antenna.

In this paper, experimental range–height indicator (RHI) X-band data from the SHV dual-polarized Taiwan Experimental Atmospheric Mobile-Radar (TEAM-R), owned and operated by the National Central University (NCU) of Taiwan are used to demonstrate the effects of aligned and canted ice particles on Z_{dr}^{shv} and ϕ_{dp}^{shv}. The data were gathered as part of the Terrain-Influenced Monsoon Rainfall Experiment (TiMREX) in southern Taiwan close to where S-Pol was deployed. TEAM-R was located roughly 25 km north of S-Pol, and thus FHV S-Pol data are used to augment and corroborate the TEAM-R data. In the ice-phase region, TEAM-R measures Z_{dr}^{shv} of about 2 dB, whereas S-Pol data show that the intrinsic Z_{dr} is close to 0 dB. From the combination of these datasets, microphysical inferences are made. In addition, a TEAM-R vertical-pointing dataset is shown for which it is likely that aligned ice particles were present over the radar, which caused the distinctive Z_{dr}^{shv} and ϕ_{dp}^{shv} features. Modeled data are given that simulate the experimental observations.

In Hubbert et al. (2014), polarimetric signatures from both SHV and FHV data gathered by S-Pol from TiMREX are used to draw similar conclusions, and T-matrix scattering calculations are also given there to support the inference that smaller electrically aligned ice crystals are responsible for the SHV Z_{dr} radial bias streaks seen in the ice phase.

This paper is organized as follows. Section 2 shows modeled data that are used to explain the experimental polarimetric signatures. Section 3 presents a TEAM-R RHI dataset that illustrates the effects of cross coupling at X band. Collocated S-Pol data are used in combination with the TEAM-R data to make microphysical interpretations. In section 4, a TEAM-R vertical-pointing dataset shows interesting polarimetric signatures that are likely due to aligned ice crystals. Conclusions and a summary are given in section 5.

2. Modeling SHV data

Modeling of SHV Z_{dr} has been done in Ryzhkov and Zrnić (2007) and Hubbert et al. (2010a,b). Ryzhkov and Zrnić (2007) showed modeling for $\pm 30°$ mean canting angle of the propagation medium over a specific range (i.e., 7–33 km). They also argued that equioriented dendritic-particle ice crystals (which caused significant specific differential phase K_{dp}) coexisted with polarimetrically isotropic snow aggregates. In their model, the aggregates had a reflectivity that was 10 dB larger than the dendritic ice crystals. Thus, the snow aggregates effectively cause the intrinsic Z_{dr} of the composite distribution to be nearly 0 dB. The aggregates do not affect the K_{dp} or the differential attenuation A_{dp} characteristics of the propagation medium. Also, their initial differential transmit phase was either 0° or $\pm\pi/2$. The motivation was to specifically mimic their experimentally observed Z_{dr} profiles. The modeling here is more like that given in Hubbert et al. (2010a,b) and Hubbert and Bringi (2003), and it is meant to aid interpretation of general SHV gathered data. We show the behavior of SHV Z_{dr} and SHV ϕ_{dp} over a range of mean canting angles and a range of transmit differential phases. Instead of modeling snow aggregates coexisting with aligned ice crystals, we simply let the backscatter medium be composed of spherical scatterers while the propagation medium is composed of canted ice crystals, which yields nearly identical modeling results, as in Ryzhkov and Zrnić (2007). Because spheres have an intrinsic Z_{dr} of 0 dB, any nonzero-decibel Z_{dr} resulting from the model is solely due to the effects of the propagation medium. If the backscatter medium does possess an intrinsic Z_{dr}, it would be added to the modeled biased Z_{dr}^{shv} value. Thus, the modeling presented here shows the isolated effects of cross coupling so that the results can be applied to general observations. Cross coupling at backscatter can affect ϕ_{dp}^{shv} if the backscatter medium is dominated by aligned ice crystals. This effect is addressed in the appendix.

Because the propagation scattering is coherent (Bringi and Chandrasekar 2001), forward scattering is completely characterized by absolute attenuation A_h, A_{dp}, and ϕ_{dp} in the 2×2 propagation scattering matrix in the polarization basis, where the 2×2 scattering

matrix is diagonal (i.e., eigen polarization basis; Bringi and Chandrasekar 2001). Mean canting angles are accounted for in the model by a Cartesian rotation of the diagonal scattering matrix. The ϕ_{dp} in the eigenpolarization bases is what mathematically causes the Z_{dr} biases to vary in SHV mode operations, and it is called principal plane ϕ_{dp} or ϕ_{dp}^{pp}. Thus, while it may be of interest to estimate the variance of the canting angles of the particles in the propagation medium, in terms of modeling the cross coupling, it is the mean canting angle and the amount of accumulated ϕ_{dp}^{pp} that control the amount of cross coupling. The ϕ_{dp}^{pp} can be thought of as the intrinsic ϕ_{dp} of the medium for waves incident at the canting angle θ, while ϕ_{dp}^{shv} (or ϕ_{dp}^{fhv}) is the ϕ_{dp} at horizontal incidence regardless of θ. In accord with this, it is most instructive to model SHV Z_{dr} bias as a function of ϕ_{dp}^{pp} with the mean canting angle θ of the propagation medium as a parameter.

The details of the radar scattering model are found in Hubbert and Bringi (2003) and Hubbert et al. (2010a). The antenna polarization errors are included in the general model, but their effects are negligible here in comparison with the cross coupling caused by the canted ice particles. For the propagation medium, the X-band differential attenuation can be variable in the ice phase (Herman and Battan 1961; Aydin et al. 1984), and we let $\alpha_{dp} = 0.001\ \text{dB}\ (^\circ)^{-1}$, where $A_{dp} = \alpha_{dp} K_{dp}$. Our scattering calculations show that α_{dp} can attain this value for larger-axis-ratio ice particles at warmer temperatures. The warmer temperature could occur from rapid ice crystal growth and latent heat release. Also there may be a quasi-liquid layer associated with the ice crystals as discussed below that would increase α_{dp}. In any case, an α_{dp} of $0.001\ \text{dB}\ (^\circ)^{-1}$ is very small and affects the scattering calculations minimally.

First, as a point of reference, simulated Z_{dr}^{fhv} and ϕ_{dp}^{fhv}, which are considered to be bias-free data, are plotted versus principal plane ϕ_{dp} and are shown in Fig. 1. Each curve corresponds to a mean θ, as given in the plots. In Fig. 1a the Z_{dr}^{fhv} curve for $\theta = 0^\circ$ begins at 0 dB and decreases linearly as specified by the assumed α_{dp}, $0.001\ \text{dB}\ (^\circ)^{-1}$. When θ is changed to 90°, the corresponding curve increases by $0.001\ \text{dB}\ (^\circ)^{-1}$. When $\theta = \pm 45^\circ$, the propagation medium is symmetrical for H and V transmit polarization so that the Z_{dr}^{fhv} is 0 dB independent of ϕ_{dp}^{pp} and A_{dp}. The other curves corresponding to $\theta = \pm 22.5^\circ$ and $\pm 67.5^\circ$ are bounded by these curves as shown. The curves for ϕ_{dp}^{fhv} in Fig. 1b are explained similarly. For $\theta = 0^\circ$, $\phi_{dp}^{fhv} = \phi_{dp}^{pp}$; for $\theta = 90^\circ$, $\phi_{dp}^{fhv} = -\phi_{dp}^{pp}$; for $\theta = \pm 45^\circ$, $\phi_{dp}^{fhv} = 0$; and the other curves in the plot are bounded by these curves as shown. Again, Fig. 1 represents what an ideal FHV dual-polarization radar would measure and is considered to be bias free. The curves are independent of the differential transmit phase $\arg\{E_v^t E_h^{t*}\}$. For FHV data, this phase is irrelevant; SHV data are significantly affected, however.

Figures 2 and 3 show the modeled SHV dual-polarization variables Z_{dr}^{shv} and ϕ_{dp}^{shv}, respectively, with the mean canting angle of the propagation medium as a parameter. Figures 2a–f are for $\arg\{E_v^t E_h^{t*}\} = 0^\circ$, 30°, 60°, 90°, 120°, and 150°, respectively. The polarization state of the transmitted field, specified by $\arg\{E_v^t E_h^{t*}\}$, can also be equivalently defined by the tilt and ellipticity angles of the transmit polarization ellipse (Azzam and Bashara 1989; Hubbert 1994). For reference, the corresponding tilt angle α and ellipticity angle ϵ of the transmit polarization ellipse are given in Table 1. The differences between the SHV Z_{dr} curves in Fig. 2 when compared with the FHV curves of Fig. 1 are due to the cross coupling of the H and V components in the SHV data. Only one set of curves is shown for ϕ_{dp}^{shv} in Fig. 3, where $\arg\{E_v^t E_h^{t*}\} = 0^\circ$. For each value of $\arg\{E_v^t E_h^{t*}\}$, the shape of the ϕ_{dp}^{shv} curves is nearly identical, only differing by a phase offset specified by $\arg\{E_v^t E_h^{t*}\}$.

Observations and interpretation

Figure 2a shows modeled Z_{dr}^{shv} when the transmit differential phase is zero. The curves for $\theta = 0^\circ$, $\pm 45^\circ$, and 90° are identical to the same θ curves of the FHV modeled data of Fig. 1. The other curves in Fig. 2a show a Z_{dr} bias from ± 0.135 to ± 0.16 dB when $\phi_{dp}^{pp} = 15^\circ$. Figure 2a curves corresponding to $\theta = \pm 45^\circ$ are identically zero because of the symmetry of the propagation medium *and* since $\arg\{E_h^t E_h^{t*}\} = 0^\circ$; in contrast, because of the nonzero phase difference between E_h^t and E_v^t, the curves for $\theta = 45^\circ$ in Figs. 2b–f show the largest $|Z_{dr}|$ bias values. In general, the largest $|Z_{dr}^{shv}|$ values are found in Fig. 2d where $\arg\{E_v^t E_h^{t*}\} = 90^\circ$ (circular transmit polarization). The transmit differential phase can also take on negative values (corresponding to negative ellipticity angles). For all of the curves in Fig. 2, if $\arg\{E_v^t E_h^{t*}\}$ is changed to $\arg\{E_v^t E_h^{t*}\} - \pi$ and if θ is changed to $-\theta$, the Z_{dr} curves remain valid. The ϕ_{dp}^{shv} curves of Fig. 3 are not affected by the change in ellipticity sign except for the phase offset, $\arg\{E_v^t E_h^{t*}\} - \pi$. An examination of Figs. 2c and 2d and Fig. 3 for $\theta = \pm 45^\circ$ shows that large biases in Z_{dr}^{shv} occur while there is very little increase in ϕ_{dp}^{shv}. Indeed, this is what is observed in the experimental data shown below.

Figures 2 and 3 also demonstrate that it is possible to determine the approximate mean canting angle of the particles in the propagation medium *if* the $\arg\{E_v^t E_h^{t*}\}$ is known. The ϕ_{dp}^{shv} curves for $\theta = \pm 67.5^\circ$ are decreasing for increasing ϕ_{dp}^{pp}, whereas for $\theta = \pm 22.5^\circ$ the ϕ_{dp}^{shv} curves are increasing. In contrast, the Z_{dr}^{shv} is positive for $\theta = 67.5^\circ$ and 22.5° and is negative for $\theta = -67.5^\circ$ and -22.5°.

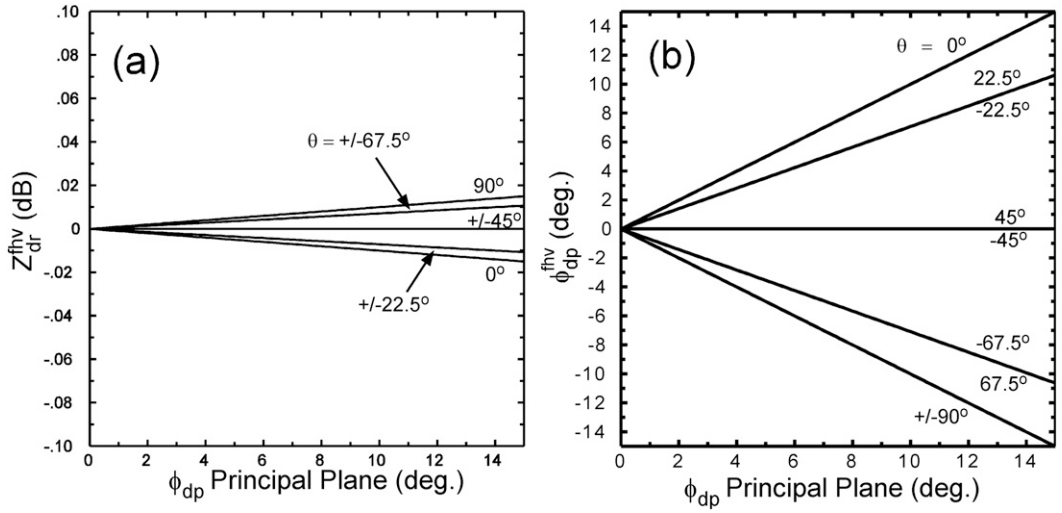

FIG. 1. FHV modeled data: (a) Z_{dr} (dB) and (b) ϕ_{dp} (°) as a function of ϕ_{dp}^{pp}, with the mean canting angle θ of the precipitation particles as a parameter. These curves are independent of the differential transmit phase $\arg\{E_v^t E_h^{t*}\}$.

The radar transmit phase is typically unknown but can be measured with an external test horn in the far field.

The reader may question why differential transmit phase should affect Z_{dr}^{shv} in such a significant way. Again, as the transmitted wave propagates, some of the H-polarization component "leaks" to the V-polarization component and vice versa because of the nondiagonal propagation matrix (i.e., canted ice crystals). This leaked signal is then coherently summed with the primary H or V signal. The two summed signals can either reinforce each other (e.g., the summed waves are in phase) or they can be destructive (e.g., they are out of phase with each other) depending on their phase relationship, which is governed by the transmit differential phase and the amount of accumulated ϕ_{dp}^{pp}. Thus, if the transmitted wave travels through a rain medium and accumulates differential phase $\phi_{dp}^{(a)}$ before the wave enters the ice phase, the effective transmit differential phase is then $\arg\{E_v^t E_h^{t*}\} + \phi_{dp}^{(a)}$.

A caveat should be added concerning the phase plot of Fig. 3. The results are applicable to the experimental data discussed below; Fig. 3 can change significantly, however, if the backscatter medium is composed *solely* of aligned and canted precipitation particles with significant axis ratios. This effect is discussed in the appendix.

3. TEAM-R RHI data

The X-band TEAM-R is Taiwan's first mobile meteorological radar and was developed under a joint project issued to three institutes in Taiwan, the NCU, the National Taiwan University, and the Chinese Culture University. After completing its construction in March of 2008, TEAM-R participated the Southwest Monsoon Experiment (SoMEX), of which TiMREX was a part, that was conducted from May to June of 2008 in southern Taiwan where it was deployed close to S-Pol. Its basic specifications are listed in Table 2. Dual polarization is achieved by transmitting and receiving H- and V-polarized waves simultaneously.

The radar data are calibrated using a combination of vertical-pointing data and the principal of self-consistency (Vivekanandan et al. 2003). Vertical-pointing data in light rain are used to calibrate Z_{dr} in standard fashion (Bringi and Chandrasekar 2001). Then the principle of self-consistency is used to calibrate H-polarization reflectivity Z_h while taking attenuation into account. Possible antenna polarization errors are not considered in this calibration process.

Two sets of TEAM-R data are shown next: 1) RHI sector data accompanied by S-Pol data and 2) vertical-pointing data. Both datasets manifest interesting anomalies that are likely due to aligned and canted ice crystals.

X-band RHI data with S-Pol data

Both TEAM-R and S-Pol data were gathered at ~0249 UTC 14 June 2008 in southern Taiwan. TEAM-R was located 3.6 km east and 29.12 km north of S-Pol, which was located at 22.5258°N, 120.4325°E. On this day a mei-yu front approached Taiwan from the northwest. Convective cells formed ahead of the mei-yu front, just west of S-Pol, and propagated to the northeast, driven by widespread winds out of the southwest. We examine one of those convective cells.

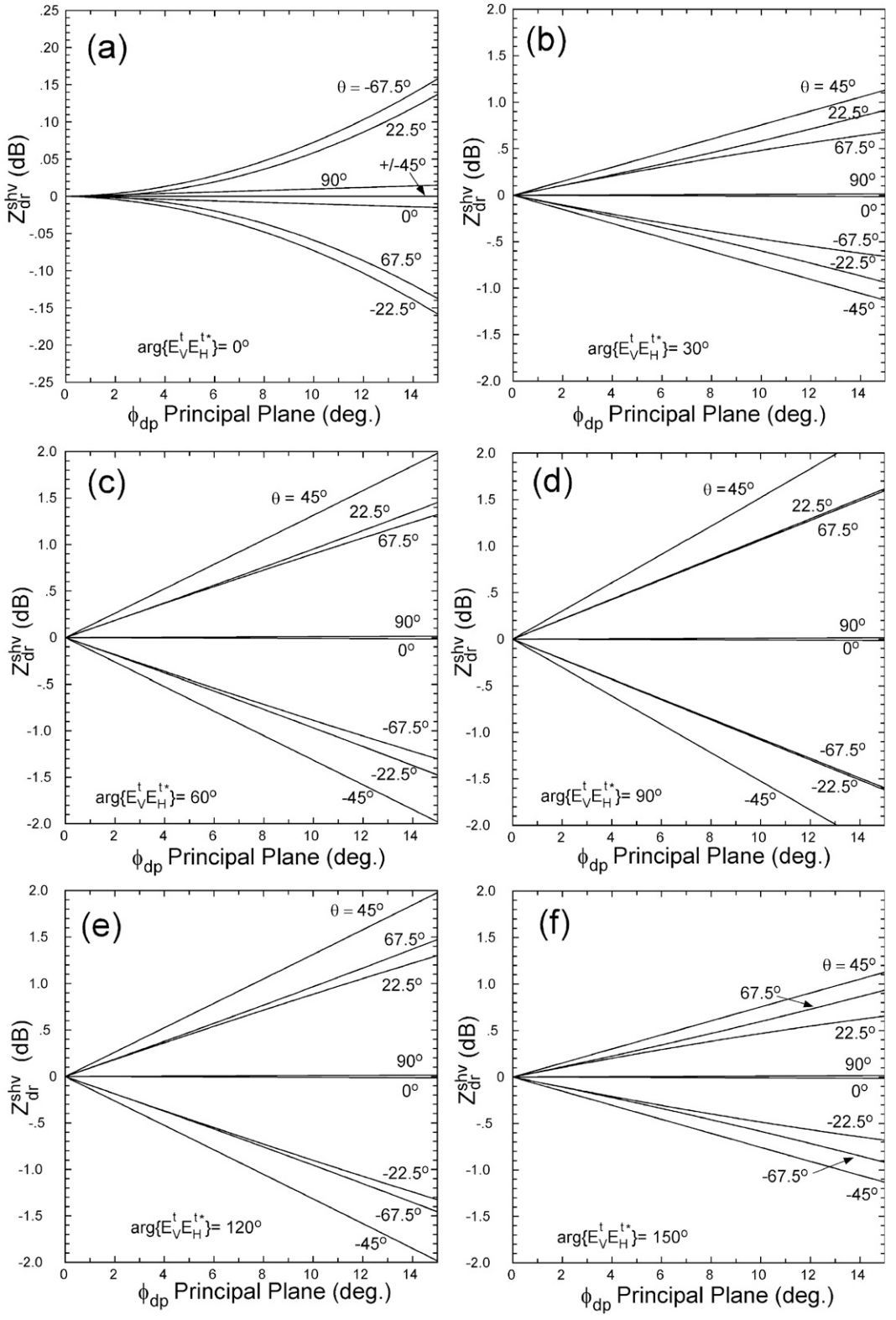

FIG. 2. SHV Z_{dr} modeled data as a function of ϕ_{dp}^{pp} with θ as a parameter. The differential transmit phase $\arg\{E_v^t E_h^{t*}\}$ is shown in each panel. Note that the curves in (a) for $\theta = 0°$, $\pm 45°$, and 90° are identical to the same curves for FHV Z_{dr} of Fig. 1. Thus, the bias in SHV Z_{dr} for $\theta = 0°$, $\pm 45°$, and 90° only becomes apparent if there is significant nonzero differential transmit phase.

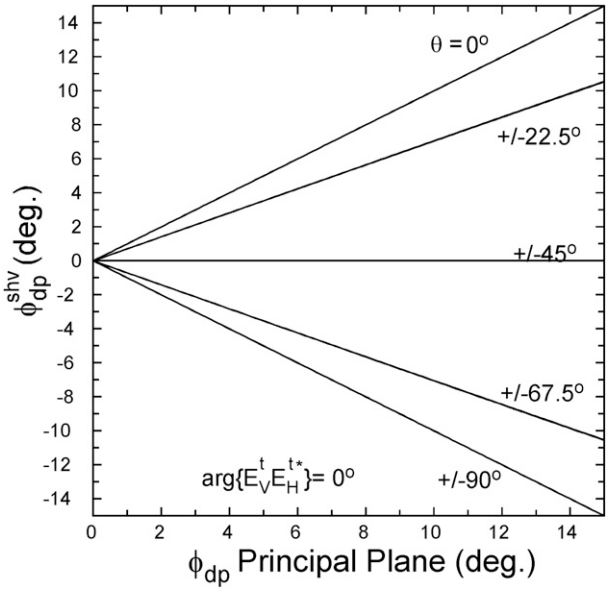

FIG. 3. SHV ϕ_{dp} modeled data as a function of ϕ_{dp}^{pp} with θ as a parameter. The differential transmit phase $\arg\{E_v^t E_h^{t*}\}$ is zero. For other values of $\arg\{E_v^t E_h^{t*}\}$, the curves are nearly identical. The only discernible difference is that each set of curves starts at $\arg\{E_v^t E_h^{t*}\}$.

To aid in the microphysical interpretations of the radar data, thermodynamic profiles are available from nearby sounding data taken in support of TiMREX. Figure 4 is a skew T plot from sounding data gathered at 0300 UTC at the Ping-Tung site, located 3.76 km east and 18.16 km north from S-Pol. The black and blue solid lines indicate the temperature and dewpoint temperature (°C), respectively, and the red dashed line is the estimated temperature (°C) of a convective parcel. The estimated convective available potential energy (CAPE) is 2154 J, with a lifted index at 500 hPa of approximately −6°C, which is sufficient to support the observed deep convection and cloud electrification. Deep moisture is evident, with the 0°C level close to 5 km AGL, as is typical in tropical environments. Figure 5 is a topographic map of southern Taiwan showing the locations of S-Pol, TEAM-R, and the Ping-Tung sounding site.

Figure 6 shows S-Pol plan position indicator (PPI) sector scan data, radar reflectivity factor Z_h (dBZ), Z_{dr}, K_{dp}, copolar correlation coefficient ρ_{hv}, and LDR as labeled, gathered from 0246:48 to 0254:40 UTC. Figure 6a shows Z_h at 1.6° elevation angle while Fig. 6b is Z_h at 8.7° elevation angle. The reflectivity data for the lower elevation angle are included to show the structure of the storm complex at near-surface levels. A line of convective cells just north of S-Pol extends to the northeast ahead of the mei-yu front, which is farther to the northwest, out of

TABLE 1. A comparison of differential transmit phase $\arg\{E_v^t E_h^{t*}\}$ and the corresponding transmit polarization ellipse parameters of tilt angle α and ellipticity angle ϵ. The H and V transmit powers are equal. The ∅ denotes "don't care," i.e., the variable may take on any value.

$\arg\{E_v^t E_h^{t*}\}$ (°)	α (°)	ϵ (°)
0	45	0
30	45	15
60	45	30
90	∅	45
120	−45	30
150	−45	15
180	−45	0
−30	45	−15
−60	45	−30
−90	∅	−45
−120	−45	−30
−150	−45	−15

view. A black "X" marks the location of TEAM-R while a dashed blue line marks the location of the X-band RHI data shown below. Data in Figs. 6b–f are from the 8.7°-elevation PPI scan that began at about 0249:37 UTC (the TEAM-R RHI data below were collected at 0249:44 UTC). Note the negative K_{dp} area in Fig. 6d at (12 km, 40 km) with a minimum of roughly $-0.4°\,km^{-1}$, which is evidence of vertically aligned ice crystals caused by storm electrification (Hendry and Antar 1982; Caylor and Chandrasekar 1996; Metcalf 1995; Krehbiel et al. 1996). Surrounding the negative K_{dp} region is a large area with positive K_{dp}, which indicates the presence of ice crystals with significant axis ratios that are likely horizontally aligned because of aerodynamic forces (Cho et al. 1981).

Both ρ_{hv} and LDR data indicate the location of the melting level by low values in ρ_{hv} and high LDR in the 25–32-km range. Other low ρ_{hv} values corresponding to high LDR values beyond the melting layer are mostly caused by low signal-to-noise ratio (SNR), but some very high LDR values are likely caused by sidelobe signal from ground clutter (Taiwan mountains and foothills).

Shown in Figs. 7a–e is a 32° azimuth RHI of TEAM-R SHV Z_h, Z_{dr}, K_{dp}, ϕ_{dp}, and ρ_{hv} data, respectively, collected at 0249:44 UTC from along the dashed blue line of Fig. 6. There is a small convective core at the 7–15-km range with Z_h exceeding 50 dBZ. The melting level can be identified by the band of high Z_{dr} and low ρ_{hv} at about 4.5 km AGL. The sounding data of Fig. 4 show that the 0°C isotherm is at 4.8 km AGL.

In Fig. 7b there is a radial red stripe of high Z_{dr}^{shv} (~1.75-dB average) in the ice phase starting at about 7 km AGL; the increasing trend in Z_{dr}^{shv} starts at roughly 6 km AGL, however, and this is where the noticeable bias in Z_{dr} that is due to cross coupling begins. Three solid black radial lines, labeled (x), (y), and (z), mark

TABLE 2. Specifications for the TEAM-R.

Characteristic	Specification
Operated by	NCU Taiwan
Platform	Mobile flatbed truck
Transmitter	Klystron
Transmitter frequency	9.620 GHz
Transmitter wavelength	3.12 cm (X band)
Transmitter peak power	50 kW
Transmitter pulse width	1μ; 1.5μ; 2μ
Pulse repetition frequency	3000 Hz (max)
Polarization diversity	H; V
Transmitted pulse package	Up to 4 pulse width
Antenna type	Parabolic reflector
Antenna diameter	1.8 m
Antenna beamwidth	1.4°
Antenna gain	42 dB
Antenna scan rate	Max: 20° s^{-1}
Receiver bandwidth	10 MHz
Receiver dynamic range	92–102 dB
Measurement range	100 km

this area of interest. Between lines (x) and (z) is a region of Z_{dr}^{shv} data that are likely biased by cross coupling, with line (y) marking the center of the most biased data. Two horizontal lines connect lines (x) and (z) and together define a trapezoidal region, termed the aligned canted ice region (ACIR), in which Z_{dr}^{shv} increases from approximately 0.1 dB to an average value of 1.75 dB along the center radial line (y). Above the top horizontal line along radial line (y), Z_{dr}^{shv} remains fairly constant at roughly 1.75 dB and then becomes noisy toward cloud top where the SNR becomes low. The ACIR of increasing Z_{dr}^{shv} is where most of the cross coupling takes place that biases the measured Z_{dr}. For reference, these lines are transferred onto the other panels in Fig. 7. The inference is that the X-band biased Z_{dr}^{shv} data are caused by ice particles with significant axis ratios that are aligned and canted relative to the radar plane of polarization in the ACIR.[1] We note that the negative radial streak of TEAM-R Z_{dr}^{shv} at ~5° elevation angle is caused by horizontal power lines that were less than 50 m from the radar.

For comparison, Fig. 8 shows a vertical cross section of S-Pol data created along the blue dashed line in the PPI sector scans shown in Fig. 6. The black lines defining the ACIR of Fig. 7 are overlaid on to the S-Pol vertical section plots. The X-band and S-band Z_h are very similar with peak Z_h of about 35 dBZ in the ACIR. When comparing Z_h values below about 15° elevation angle, however, the X-band Z_h is heavily attenuated by the heavy rain beyond roughly 15 km range. Figure 7d shows that the total accumulated X-band ϕ_{dp}^{shv} is ~40° in the area marked in red from the color scale. If the absolute attenuation is 0.3 dB $(°)^{-1}$ (Park et al. 2005; Bringi et al. 1990), then the attenuation in the X-band Z_h is 12 dB in this area, although our focus in this paper is not attenuation correction. In a similar way, if $\alpha_{dp} = 0.03$ dB $(°)^{-1}$ (a reasonable value for rain at X band), then Z_{dr}^{shv} is biased by −1.2 dB. Figure 7b shows that the effects of differential attenuation extends up to 6 km AGL from 17- to 25-km range (area in green from the color scale). In contrast, there is little ϕ_{dp}^{shv} increase through the region between the lines (x) and (z) below the ACIR. The S-Pol Z_{dr} data show that the intrinsic Z_{dr} in the ice-phase region of the TEAM-R RHI is generally close to zero and is somewhat positive, mostly ranging from ~0 to 0.3 dB. It is important to note that the S-Pol Z_{dr} shows no evidence of the Z_{dr}^{shv} streaks seen in the TEAM-R data.

The TEAM-R and S-Pol K_{dp} display similar features. Both show a region of negative K_{dp} on the right-hand side of the ACIR with minimums of about $-0.3°\,km^{-1}$ at S band and $-2.5°\,km^{-1}$ at X band. The difference between the X-band K_{dp} and S-band K_{dp} is approximately a factor 3.5 because of the wavelength difference between the two radars. The X-band K_{dp} here exceeds that estimate, possibly because of the X-band data's much finer spatial resolution and different K_{dp} filter characteristics. Also, the X-band and S-band data are not exactly collocated in space and time. Further, the TEAM-R and S-Pol radars are not collocated, and thus their viewing angles of their corresponding resolution volumes are different. All of these factors make precise comparisons difficult, but the S-Pol and TEAM-R viewing angles and resolution volumes are sufficiently close to allow qualitative data comparisons.

MICROPHYSICAL INTERPRETATION OF RADAR MEASUREMENTS

The X-band and S-band radar data together with the modeling from section 2 and the modeling results of Hubbert et al. (2014) provide the basis for microphysical interpretation of the particles in the ACIR and surrounding area. Figures 7c and 8d show negative K_{dp} in the ACIR and to the right of the ACIR from −0.3° to $-0.4°\,km^{-1}$ for the S-band data and from −0.5° to $-1.5°\,km^{-1}$ for the X-band data. There are also positive K_{dp} values along line (x): from 0.4° to $0.6°\,km^{-1}$ for the S-band data and from 0.5° to $2°\,km^{-1}$ for the X-band data. S-Pol data in Figs. 6c and 8b indicate that the intrinsic Z_{dr} in the ice phase around the X-band RHI is roughly 0–0.3 dB, and thus the anomalous high X-band

[1] The ice particles are canted relative to the horizontal axis of the plane of polarization of the radar. The plane of polarization is perpendicular to the line of site of the radar. Thus, the orientation of the ice particle is projected onto the plane of polarization, creating the apparent canting angle.

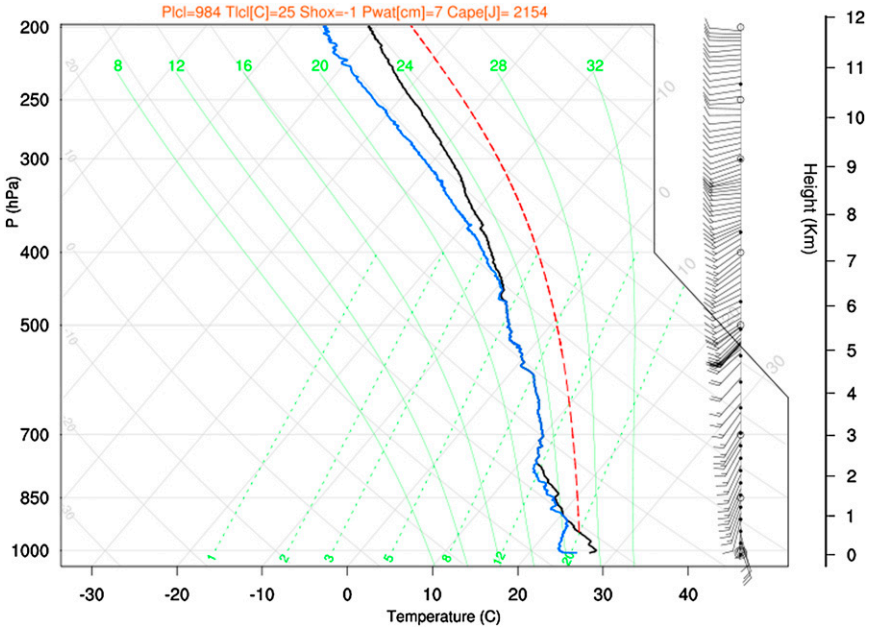

FIG. 4. A skew T plot from sounding data taken at the Ping-Tung (sometimes called Ping-Dong) site located 3.76 km east and 18.16 km north from S-Pol at 0300 UTC. The black and blue solid lines indicate the temperature and dewpoint temperature (°C), respectively, and the red dashed line is the estimated temperature (°C) of a convective parcel.

Z_{dr}^{shv} values are indeed artifacts. Also, the reflectivities in the ACIR are very high for ice: mostly in the 20–35-dBZ range. From T-matrix scattering calculations in Hubbert et al. (2014; their Tables 1 and 2), ice particles that can yield values from $\pm 0.3°$ to $\pm 0.6° \text{ km}^{-1}$ would also yield Z_{dr} values from ± 2.5 to ± 5 dB. Also, for the particle concentration considered in Hubbert et al. (2014), the Z_h would be in the 10–18-dBZ range as compared with the 20–35 dBZ observed here. From this result, we infer that there are two types of ice particles coexisting in the ACIR and surrounding region: 1) ice crystals that are aligned with significant axis ratios that give the observed high $|K_{dp}|$ and 2) polarimetrically isotropic larger ice particles (graupel or aggregates) that give the higher observed reflectivity and the near-zero-decibel Z_{dr} (Hubbert et al. 2014; Ryzhkov and Zrnić 2007; Kennedy and Rutledge 2011). Because there is a significant region with negative K_{dp}, we infer that charge separation has taken place that has caused the ice crystals' major axes to be aligned close to vertical. The lightning detection network of Taiwan did record numerous electrical discharges in the general storm complex, as shown by the blue times signs in Fig. 6b.

Around line (y), both X-band ϕ_{dp}^{shv} and K_{dp}^{shv} show that there is little phase shift occurring as the wave propagates through the ACIR. This then indicates that the hypothesized smaller aligned ice crystals possess a mean canting angle of roughly 45° relative to the polarization plane of the radar. To use the Z_{dr}^{shv} and ϕ_{dp}^{shv} model plots of Figs. 2 and 3, the amount of *principal plane* ϕ_{dp} through the ACIR needs to be estimated. Figure 7d shows ϕ_{dp}^{shv} and not ϕ_{dp}^{pp}. To estimate the amount of ϕ_{dp}^{pp}

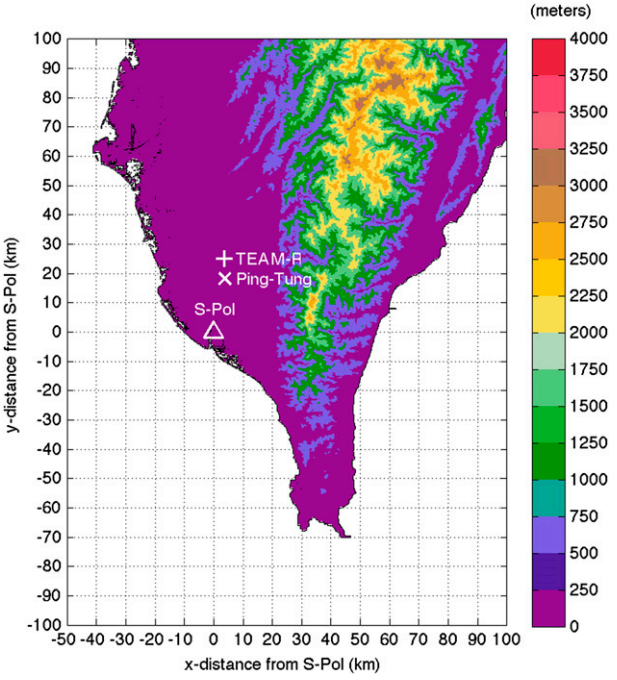

FIG. 5. A topographic map of southern Taiwan showing the locations of S-Pol, TEAM-R, and the Ping-Tung sounding site.

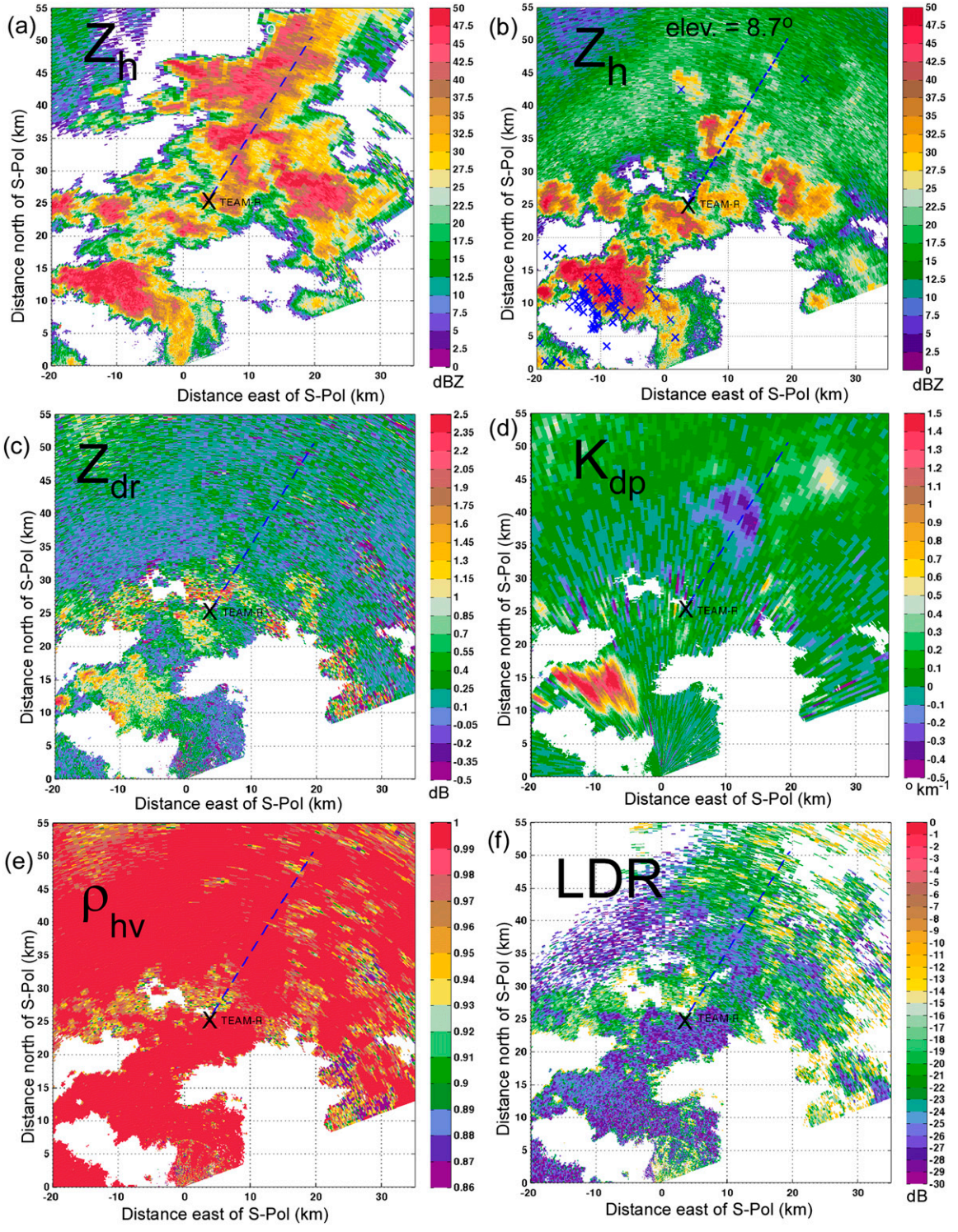

FIG. 6. S-Pol PPI FHV data from TiMREX collected on 14 Jun 2008: (a) Z_h from 1.6° elevation and (b)–(f) data from 8.7° elevation. The PPI sector scan began at 0246:48 and ended at 0254:40 UTC so that it encompasses the scan time of the TEAM-R RHI data in Fig. 7. The black "X" marks the location of TEAM-R while the blue dashed line shows the location of the TEAM-R RHI data of Fig. 7. The blue times signs in (b) mark the locations of electrical discharges in a ±10-min time frame around 0249 UTC, as recorded by the Taiwan lightning detection network.

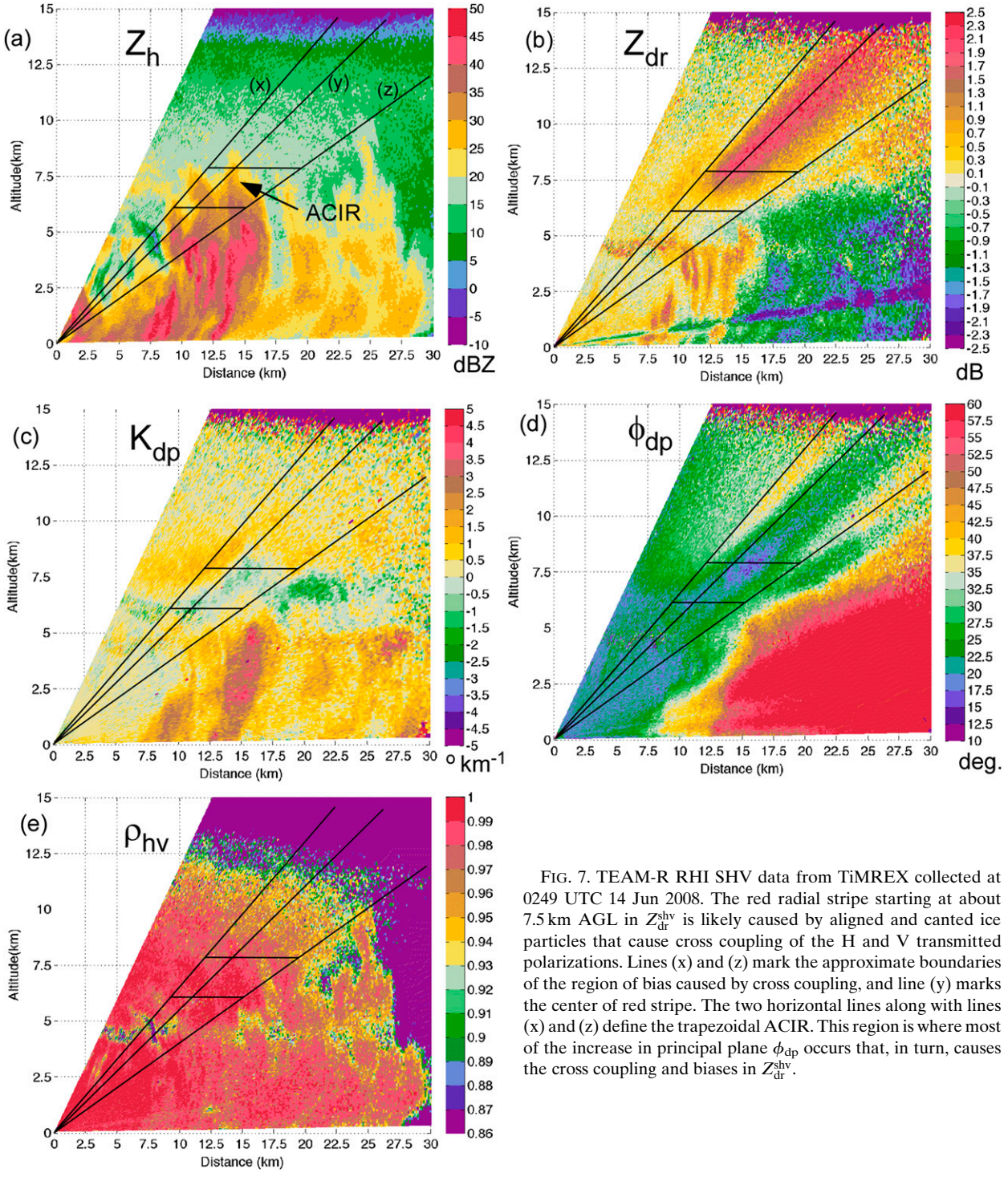

FIG. 7. TEAM-R RHI SHV data from TiMREX collected at 0249 UTC 14 Jun 2008. The red radial stripe starting at about 7.5 km AGL in Z_{dr}^{shv} is likely caused by aligned and canted ice particles that cause cross coupling of the H and V transmitted polarizations. Lines (x) and (z) mark the approximate boundaries of the region of bias caused by cross coupling, and line (y) marks the center of red stripe. The two horizontal lines along with lines (x) and (z) define the trapezoidal ACIR. This region is where most of the increase in principal plane ϕ_{dp} occurs that, in turn, causes the cross coupling and biases in Z_{dr}^{shv}.

accumulated through ACIR, the area just to the left of the two ACIR horizontal lines in Fig. 7d is used where the ice crystals are likely horizontal since there is little evidence of cross-coupling Z_{dr}^{shv} bias along these radials in the ice phase. There is approximately 7° of phase shift through this region. The vertical-pointing TEAM-R data given below indicate that the transmit differential phase for TEAM-R is around −90°. On the basis of this result, consider the Z_{dr}^{shv} model data given in Fig. 2d. To use this plot for $\arg\{E_v^t E_h^{t*}\} = -90°$ (instead of

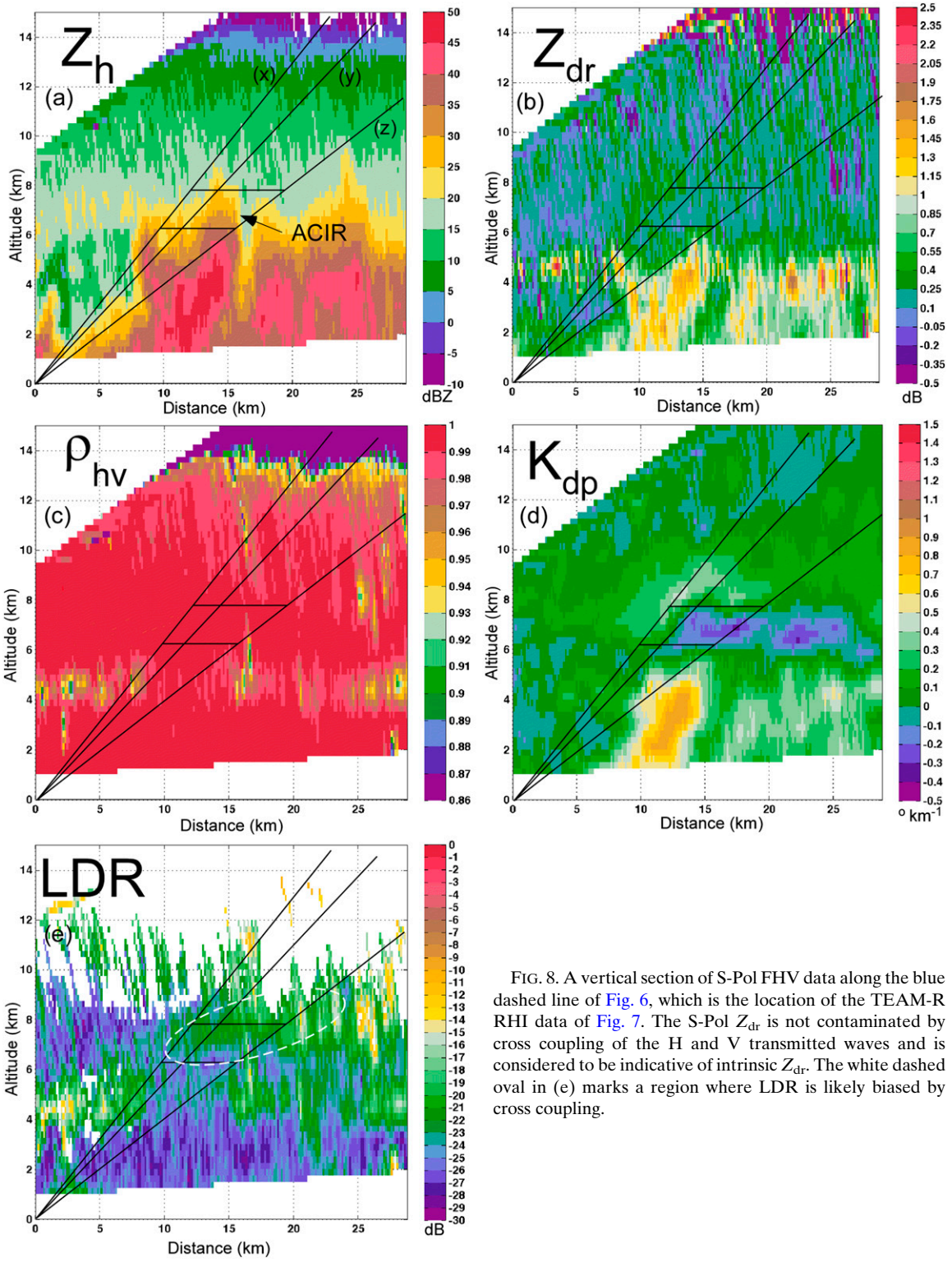

FIG. 8. A vertical section of S-Pol FHV data along the blue dashed line of Fig. 6, which is the location of the TEAM-R RHI data of Fig. 7. The S-Pol Z_{dr} is not contaminated by cross coupling of the H and V transmitted waves and is considered to be indicative of intrinsic Z_{dr}. The white dashed oval in (e) marks a region where LDR is likely biased by cross coupling.

$\arg\{E_v^t E_h^{t*}\} = +90°$), all of the given mean canting angles change sign. Thus, to have a positive Z_{dr}^{shv} cross-coupling bias, the mean canting angle needs to be negative. A mean canting angle of $-45°$ yields a Z_{dr}^{shv} bias of 1.1 dB for 7° of ϕ_{dp}^{pp}. Figures 6c and 8b indicate that the intrinsic Z_{dr} in the ACIR and above is ~0.1–0.3 dB. Adding this to the above bias estimate gives 1.2–1.4 dB for Z_{dr}^{shv}, which is short of the measured 1.75 dB. Thus, we expect

that the ϕ_{dp}^{pp} accumulation was closer to 10° so that the Z_{dr}^{shv} bias from Fig. 2d is increased from 1.1 to 1.5 dB, which is then in good agreement with the measured TEAM-R Z_{dr}^{shv} values at the top of the ACIR.

Going from left to right across the ACIR, K_{dp}^{shv} in Fig. 7c is first positive and then becomes negative. Using Fig. 2d along with Fig. 3 (again with the signs of the mean canting angles changed), we infer that the mean canting angle of the ice crystals is from approximately −22.5° to −45° on the left-hand side of the ACIR and between −45° and −67° on the right-hand side. Such information may allow for inferences about the electric fields in this region. We note that the above inference of the coexistence of two types of ice particles, smaller ice crystals with larger graupel, is considered to be favorable for charge separation from particle collisions (Workman and Reynolds 1949; Williams and Lhermitte 1983; Dye et al. 1988; Rutledge et al. 1992; Carey and Rutledge 1996; Petersen et al. 1996, 1999; Deierling et al. 2008).

Figure 8e shows S-Pol LDR data, which also can be biased by cross coupling (Ryzhkov and Zrnić 2007; Hubbert et al. 2010b). The region marked by the dashed white oval shows elevated LDR values that are likely due to canted ice crystals, which caused the TEAM-R radial Z_{dr}^{shv} bias streaks discussed above. To the right of the white oval are some high LDR values marked in yellow from the color scale, with corresponding lower values of ρ_{hv} that are likely caused by sidelobe power from ground clutter or the storm core below these areas.

It is well known that there exists a layer at the surface of ice below the bulk melting point where the water molecules are in a quasi-liquid state called the quasi-liquid layer (QLL; Li and Somorjai 2007; Dash et al. 2006). The thickness of the QLL has been estimated to be on the order of 2–100 nm (Li and Somorjai 2007; Pruppacher and Klett 1997). The possible importance of the QLL to storm electrification and crystal growth has been discussed in Dash and Wettlaufer (2003), Dash et al. (2001), and Libbrecht and Yu (2001). Sazaki et al. (2012) more recently provided advanced optical microscopy evidence of the QLL. Also, Libbrecht and Tanusheva (1998, 1999) show that electric fields can significantly accelerate crystal growth. The ACIR here is characterized by the presence of an electric field and a saturated atmosphere ranging from approximately 6.1 to 7.9 km, which corresponds to temperatures from −8° to −19°C as based on the sounding data in Fig. 4. From the radar data, it is inferred that there are many aligned smaller ice crystals in the ACIR that are likely growing rapidly in the ice supersaturated conditions. For ice crystals that are 0.5 mm with an axis ratio of 10, the smaller ice crystal dimension is then 0.05 mm. If the QLL is 100 nm, this gives a ratio of 0.05 mm/100 nm, or 500. It is possible that the QLL could affect the radar scattering characteristics of these smaller crystals (Herman and Battan 1961) by increasing their effective dielectric constant such that they enhance the observed cross-coupling Z_{dr} biases seen in the TEAM-R data above. The scattering properties of such ice crystals should be modeled, but that is beyond the scope of this paper.

4. TEAM-R vertical-pointing data

Figure 9 shows TEAM-R vertical-pointing data while the radar dish rotates 360° in azimuth angle, in stratiform rain from 0330 UTC 18 July 2008 in Taiwan. SHV Z_h, Z_{dr}, ϕ_{dp}, and ρ_{hv} are shown in the four panels. The maximum Z_h is ~35 dBZ. The bright band is clearly evident from the rings in the ρ_{hv} and Z_{dr} data just beyond the 5-km range. The high ρ_{hv} values indicate good data quality. The total precipitation echo depth, taken as the outer edge of the white-on-the-color-scale (0 dBZ) data in the Z_h panel, is approximately 15 km. The ϕ_{dp}^{shv} begins to increase/decrease at a height of roughly 1.5 km above the bright band, similar to the previous case. The ϕ_{dp}^{shv} increases in the regions around 0° and 180° azimuth and decreases in regions around 90° and 270° azimuth (0° azimuth corresponds to the vertical axes of the plots). Also note the locations of the maxima/minima of Z_{dr} data (brown/green colors) and of maximum increase/decrease of ϕ_{dp}^{shv} (green/purple colors). They do not coincide as one might intuitively think they should; that is, for FHV data, one expects the regions of maximum/minimum Z_{dr} and maximum increasing/decreasing ϕ_{dp} to more or less coincide. The model SHV data presented below explain this. It is very likely that there are aligned ice crystals above the radar that cause this signature. Even though the maximum increase in principal plane ϕ_{dp} versus height is only ~7°, modeling below demonstrates that this amount of phase shift is sufficient to cause the observed polarimetric signatures.

Modeled vertical-pointing data

Next, the radar scattering model is used to simulate the general character of the vertical-pointing data of Fig. 9. For the model, we assume the presence of columnar ice crystals with their mean major axis aligned with the horizontal axis of the radar plane of polarization when the radar azimuth angle is 0°. The ice crystals have an intrinsic Z_{dr} of 0.5 dB and an LDR of −35 dB when they are aligned with the radar's polarization axes. These values are reasonable for aligned ice crystals. Shown first for reference in Figs. 10a and 10b are the FHV variables Z_{dr}^{fhv} and ϕ_{dp}^{fhv}, which are considered to be unbiased data. The data are plotted in polar coordinates with the radial axis representing principal plane ϕ_{dp} and

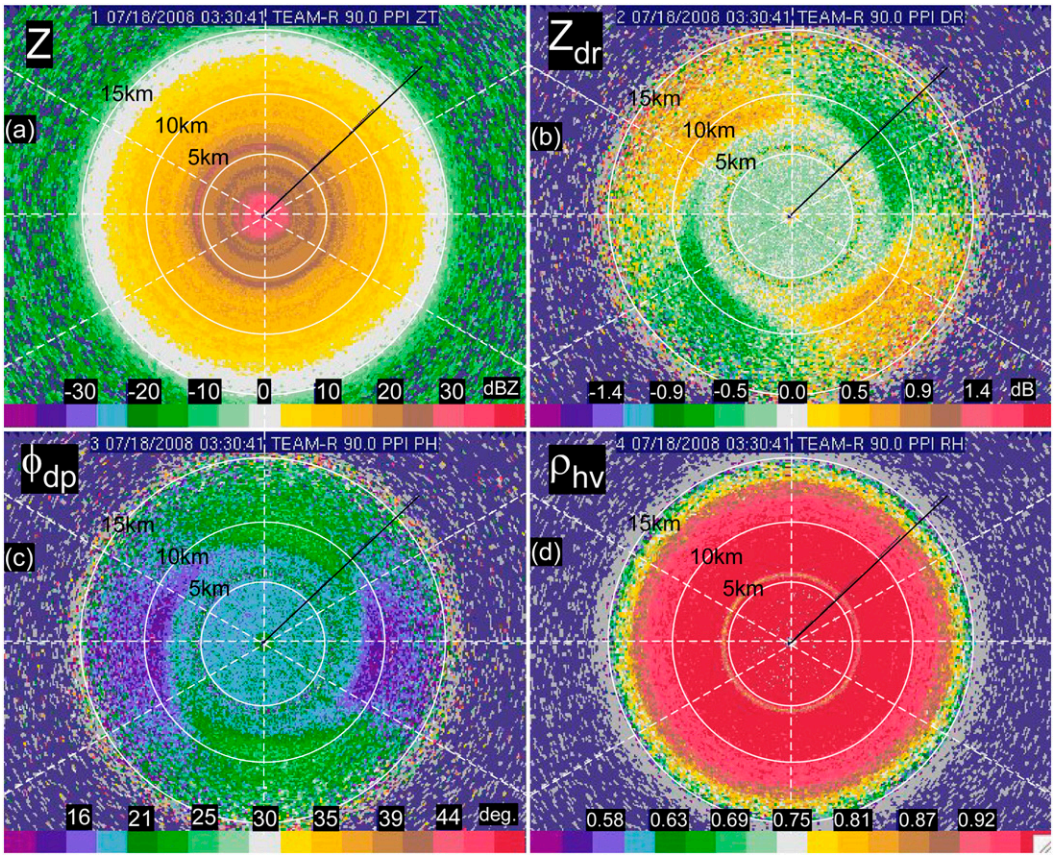

FIG. 9. Vertical-pointing SHV TEAM-R data collected at 0330 UTC 18 Jul 2008. The radar points vertically while the antenna dish rotates 360°. Thus the polar angle corresponds to the radar azimuth angle. The radial axis is distance above the radar. Note that the lines of symmetry for the maximum Z_{dr} are $\sim\pm45°$ while the lines of symmetry for maximum increase/decrease in ϕ_{dp} are roughly 0° and 90°. Cross coupling of the H and V transmitted signal caused by aligned ice crystals is likely the cause.

with the polar angle corresponding to the rotation angle (azimuth) of the radar antenna. To mimic the experimental data plots and for better data viewing, an offset of 5° was added to the ϕ_{dp}^{pp} values, and this causes the pictured inner circle of blank data. As expected, the plots are symmetric about the vertical and horizontal axes. The maximum Z_{dr}^{fhv} and ϕ_{dp}^{fhv} are along the vertical axes of Fig. 10. Note that the radial variable in the experimental data is range in kilometers, whereas the modeled data radial variable is ϕ_{dp}^{pp}. This is done for the modeled data since range is not important per se; it is the amount of ϕ_{dp}^{pp} that the transmitted wave experiences, which affects the polarization signatures. To interpret the modeled data and to compare them with the experimental data, 1° of principal plane ϕ_{dp} accumulation corresponds to roughly 1 km; that is, the specific principal plane differential phase K_{dp}^{pp} is roughly $1°\,km^{-1}$ for this case. The exact value of K_{dp}^{pp} is not important since our intent here is to show how the general character of the experimental data can be simulated. The differential attenuation again is $0.001\,dB\,(°)^{-1}$ (i.e., negligible).

Shown in Fig. 10c and 10d and Fig. 11 are the simulated Z_{dr}^{shv} (left column) and ϕ_{dp}^{shv} (right column) with transmit differential phase as a parameter: $\arg\{E_v^t E_h^{t*}\} = 0°$, 45°, 90°, and −90°, respectively. Note again from the experimental data of Fig. 9 that the Z_{dr} and ϕ_{dp} maxima/minima do not coincide with each other along radar radials as they do in the FHV modeled data in Fig. 10. This can be attributed to SHV operations along with a phase difference between the H and V transmit waves. In Figs. 10c and 10d, $\arg\{E_v^t E_h^{t*}\} = 0$ so that ϕ_{dp}^{shv} is very similar to the ϕ_{dp}^{fhv} of Figs. 10a and 10b. The accompanying Z_{dr}^{shv} does show some azimuthal distortion or "twisting" when compared with Z_{dr}^{fhv} in Fig. 10, however. In Fig. 11 with $\arg\{E_v^t E_h^{t*}\} = 45°$, 90°, and −90° from top to bottom, respectively, this twisting of both Z_{dr}^{shv} and ϕ_{dp}^{shv} is evident, and it resembles the experimental vertical-pointing data of Fig. 9. The experimental data most resemble the modeled data of Figs. 11e and 11f, and thus it is likely that

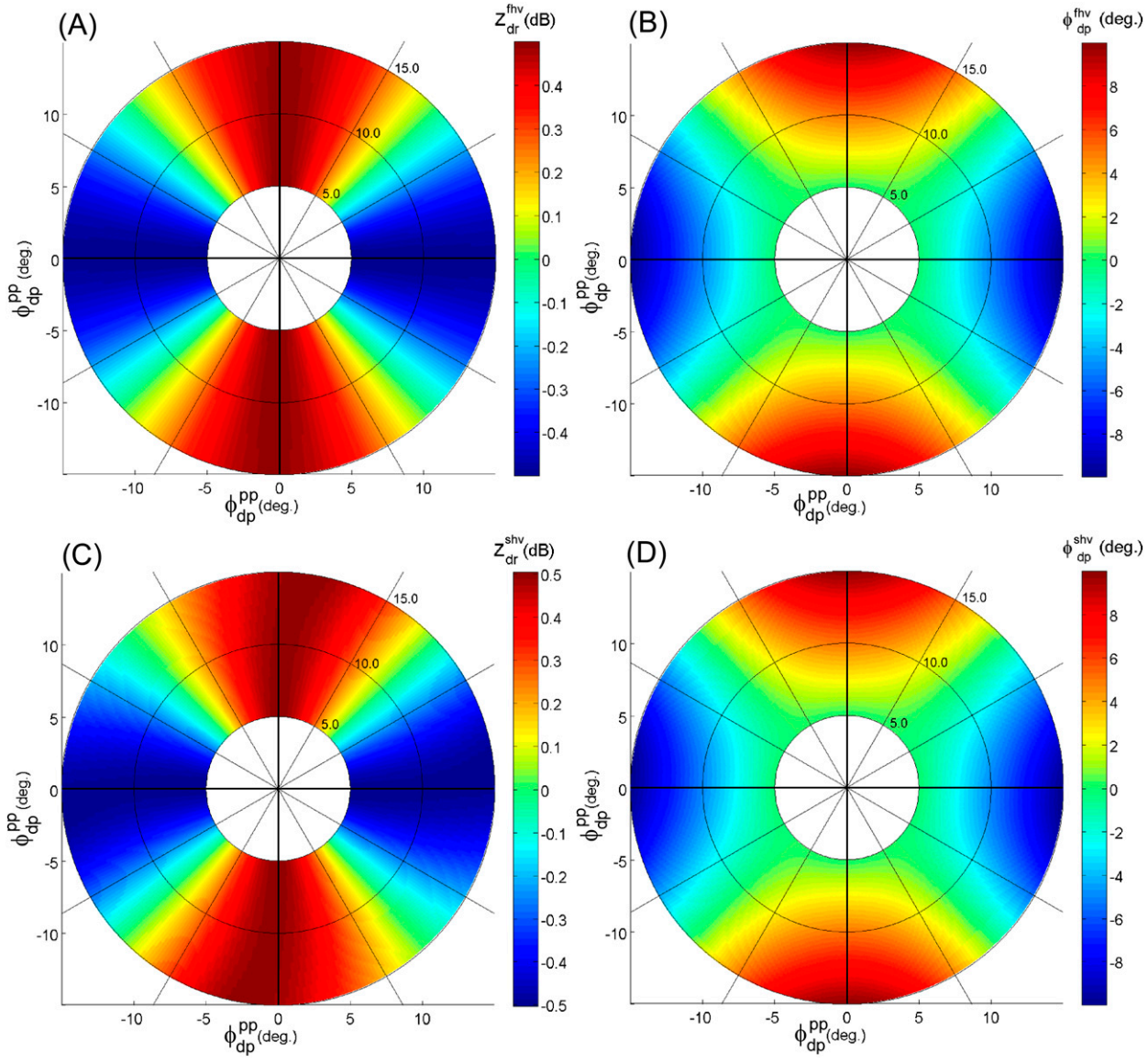

FIG. 10. The (a) Z_{dr}^{fhv} (dB) and (b) ϕ_{dp}^{fhv} (°) FHV modeled data and (c) Z_{dr}^{shv} (dB) and (d) ϕ_{dp}^{shv} (°) SHV modeled data. The polar angle is the radar azimuth rotation angle, with 0° corresponding to the vertical axis of the plots. The radial independent variable is ϕ_{dp}^{pp} in degrees. An offset of 5° has been added to ϕ_{dp}^{pp}, for viewing purposes. The FHV data are considered to be nonbiased data with which the SHV data can be compared. The purpose here is to simulate the experimental data of Fig. 9 starting from just beyond the bright band.

the TEAM-R radar possesses a negative $\arg\{E_v^t E_h^{t*}\}$ in the range from −45° to −90°.

The ϕ_{dp}^{shv} is affected by two cross-coupling mechanisms: 1) propagation and 2) backscatter. The backscatter cross coupling is described in the appendix. For Fig. 11d, ϕ_{dp}^{shv} is 86.7° when the azimuth angle is 45° (measured clockwise from the vertical axis) and ϕ_{dp}^{pp} is 5° (data at the inner most ring of Fig. 11). Nominally ϕ_{dp}^{shv} is 90° as dictated by $\arg\{E_v^t E_h^{t*}\} = 90°$ for this plot. The 86.7° results from cross coupling at backscatter. The cross-coupling effects due to propagation are evident in the data of Fig. 11 as seen from the radial variability of the plots. From Figs. 11c and 11d it is seen that even an increase of 2° in ϕ_{dp}^{pp} is sufficient to cause visible twisting of Z_{dr}^{shv} and ϕ_{dp}^{shv} signatures as observed in the experimental data of Fig. 9. The black dashed lines labeled (g) and (h) in Figs. 11c and 11d mark the radials where Z_{dr}^{shv} attains minimum [line (h)] and maximum [line (g)] values of ~±1.6 dB for $\phi_{dp}^{pp} = 15°$, a difference of –1.1 dB when compared with the intrinsic Z_{dr} of the ice crystals (±0.5 dB). In comparison, the ϕ_{dp}^{shv} of Fig. 11d shows very little change in value along lines (g) and (h).

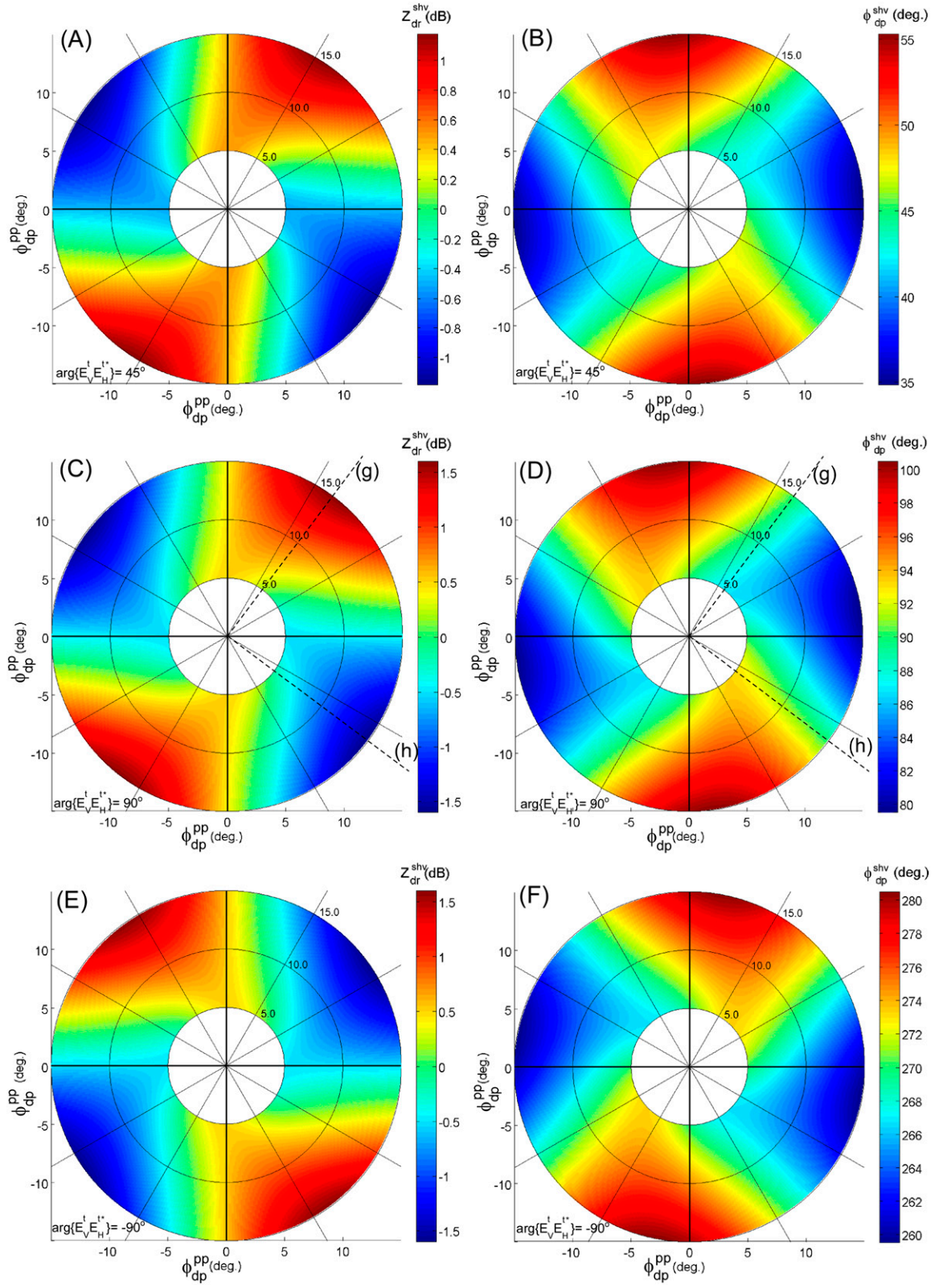

FIG. 11. SHV modeled data as in Figs. 10c and 10d: (left) Z_{dr}^{shv} (dB) and (right) ϕ_{dp}^{shv} (°) for arg$\{E_v^t E_h^{t*}\}$ = (a),(b) 45°, (c),(d) 90°, and (e),(f) −90°.

5. Summary and conclusions

In this paper, X-band experimental data, biased as a result of cross coupling of the simultaneously transmitted H and V waves caused by canted ice crystals, were presented, modeled, and interpreted. An RHI of SHV X-band data was collected in conjunction with FHV PPI S-band data during TiMREX in Taiwan. The X-band Z_{dr}^{shv} RHI plots showed a radial streak of high Z_{dr}^{shv} of ~1.75 dB in the ice phase of a convective storm. The collocated S-band data showed that the intrinsic Z_{dr} was in the 0.1–0.3-dB range. There were areas of negative K_{dp} that indicated that ice crystals were vertically oriented, very likely because of the presence of an electric field, which was supported by measurements from the Taiwan lightning detection network. An aligned and canted ice crystal region was analyzed that showed small, near-zero K_{dp} collocated with the biased X-band Z_{dr}^{shv}, suggesting that aligned ice crystals were canted at roughly 45°. Other regions showed positive K_{dp}, indicating that ice crystals were aligned with a mean canting angle that was close to horizontal. Scattering calculations indicate that ice particles with high magnitudes of K_{dp} in the ice phase would also possess high-magnitude Z_{dr}. The coincident observed near-zero values of S-band Z_{dr}^{fhv} suggested the coexistence of two types of ice particles in the radar resolution volume: 1) lower-reflectivity aligned ice crystals that yield a high K_{dp} and 2) higher-reflectivity, polarimetrically isotropic larger ice aggregates or graupel that mask the high intrinsic Z_{dr} of the aligned ice crystals while not affecting the K_{dp}.

These inferences were supported by the presented modeling plots. The modeling plots demonstrated that if the transmit differential phase ($\arg\{E_v^t E_h^{t*}\}$) is known then the approximate mean canting angle of the ice crystals causing the biased data could be roughly estimated. The transmit differential phase is due to the transmit electronics and waveguide components plus any differential phase that is accumulated in rain before the wave is incident on the ice particles. The Z_{dr}^{shv} bias will be maximum if the mean canting angle of the propagation medium is 45° *and* there is significant transmit differential phase. Thus, this demonstrates why it is of interest to measure $\arg\{E_v^t E_h^{t*}\}$ for SHV radars for data interpretation. The microphysical inferences and interpretation here are consistent with those found in Hubbert et al. (2014).

Experimental X-band vertical-pointing data from TEAM-R showed a so-called twisting of Z_{dr}^{shv} and ϕ_{dp}^{shv} versus height and azimuth angle. The azimuth angles where maximum (minimum) Z_{dr}^{shv} occurred did not correspond to where maximum (minimum) ϕ_{dp}^{shv} phase accumulation occurred, which would be the case if the radar employed FHV transmission. This was explained and demonstrated via a radar scattering model. The twisting Z_{dr}^{shv} and ϕ_{dp}^{shv} signatures are caused by cross coupling that is due to azimuthally aligned ice crystals above the radar. The shape of the twisting of the Z_{dr}^{shv} and ϕ_{dp}^{shv} data indicated that the TEAM-R data most resemble the simulated data when the transmit differential phase is −90°.

Acknowledgments. The National Center for Atmospheric Research is sponsored by the National Science Foundation. Any opinions, findings, and conclusions or recommendations expressed in this publication are those of the authors and do not necessarily reflect the views of the National Science Foundation. We thank Ms. Tracy Hertneky who created the skew T plot. We also acknowledge the staff at NCAR's Earth Observing Laboratory who set up and operated S-Pol for TiMREX. We appreciate the students from National Central University, National Taiwan University, Chinese Culture University, and National Defense University of Taiwan who operated TEAM-R during TiMREX.

APPENDIX

Cross-Coupling Effects at Backscatter from Aligned Crystals on ϕ_{dp}^{shv}

If the backscatter medium consists *solely* of prolate or oblate ice crystals with their axes aligned at a nonzero mean canting angle, ϕ_{dp}^{shv} suffers a phase shift at backscatter because of cross coupling of the simultaneously transmitted H and V waves, even for Rayleigh scatterers. In Fig. 3, the backscatter medium was allowed to be composed solely of spherical scatterers so that there is no cross coupling of the H and V waves at backscatter. This was done to mimic the behavior of the experimental data in this paper: we infer that aligned ice crystals coexist with larger, polarimetrically isotropic ice particles (e.g., graupel) that dominate the backscatter measurements. For such a mixture of ice particles, Z_{dr} is zero and LDR is also small when the graupel has near-unity axis ratios. Here we consider just the backscatter medium composed solely of aligned ice crystals and examine their effects on ϕ_{dp}^{shv}. We model the ice crystals as prolate spheroids, with an axis ratio of 2.165 (so that Z_{dr} = 3 dB). The orientation distribution is Fisher (Fisher 1953; Mardia 1972) with a mean major axis canting angle that is aligned horizontally in the radar's plane of polarization. The spread of the canting angles is specified by the κ parameter as 600, which corresponds to about 68% of the canting angles being contained in an annulus of 3.5° about the mean canting angle. The particle size distribution used is

TABLE A1. The ϕ_{dp}^{shv} for a distribution of aligned and canted ice particles with axis ratio of 2.165, selected so that the intrinsic Z_{dr} is 3 dB. The first row shows the values for the mean canting angle of the ice crystals. The $\arg\{E_v^t E_h^{t*}\} = 90°$. If $\arg\{E_v^t E_h^{t*}\} = 0°$, ϕ_{dp}^{shv} is always zero.

θ (°)	−67.5	−45	−22.5	0	22.5	45	67.5	±90
ϕ_{dp}^{shv} (°)	105	110	104	90	75	72	77	90

specified in Fig. 8 of Hubbert et al. (2014). The scattering model used is described in Hubbert and Bringi (2003) and Hubbert et al. (2010a). Table A1 shows ϕ_{dp}^{shv} for various values of the mean canting angle of the ice crystals when $\arg\{E_v^t E_h^{t*}\} = 90°$. If $\arg\{E_v^t E_h^{t*}\} = 0°$, $\phi_{dp}^{shv} = 0°$. These calculations show that, when the backscatter volume is dominated by aligned and canted ice crystals, cross coupling of the H and V waves significantly effects ϕ_{dp}^{shv}. For example, consider an SHV wave that travels through this medium in range where first $\theta = 0°$ followed by 22.5°, 45°, 67.5°, and then 90°. This would presumably occur because of the structure of the electric field. The ϕ_{dp}^{shv} would go from 90° to 75°, to 72°, to 77°, and then back to 90°, assuming negligible cross coupling on propagation. This change in phase would appear as a large perturbation in the ϕ_{dp}^{shv} range profile that possibly could be falsely interpreted as Mie-scattering effects or propagation effects. In this paper, we argue that aligned ice crystals coexist with graupel so that these backscattering cross-coupling effects are negligible.

REFERENCES

Aydin, K., T. A. Seliga, and V. N. Bringi, 1984: Differential radar scattering properties of model hail and mixed-phase hydrometeors. *Radio Sci.,* **19,** 58–66, doi:10.1029/RS019i001p00058.

Azzam, R. M. A., and N. M. Bashara, 1989: *Ellipsometry and Polarized Light.* North Holland, 558 pp.

Bringi, V. N., and V. Chandrasekar, 2001: *Polarimetric Doppler Weather Radar.* Cambridge University Press, 636 pp.

——, ——, N. Balakrishnan, and D. Zrnić, 1990: An examination of propagation effects in rainfall on radar measurements at microwave frequencies. *J. Atmos. Oceanic Technol.,* **7,** 829–840, doi:10.1175/1520-0426(1990)007<0829:AEOPEI>2.0.CO;2.

Carey, L. D., and S. A. Rutledge, 1996: A multiparameter radar case study of the microphysical and kinematic evolution of a lightning producing storm. *Meteor. Atmos. Phys.,* **59,** 33–64, doi:10.1007/BF01032000.

Caylor, I. J., and V. Chandrasekar, 1996: Time-varying ice crystal orientation in thunderstorms observed with multiparameter radar. *IEEE Trans. Geosci. Remote Sens.,* **34,** 847–858, doi:10.1109/36.508402.

Cho, H.-R., J. V. Iribarne, and W. G. Richards, 1981: On the orientation of ice crystals in a cumulonimbus cloud. *J. Atmos. Sci.,* **38,** 1111–1114, doi:10.1175/1520-0469(1981)038<1111:OTOOIC>2.0.CO;2.

Dash, J. G., and J. S. Wettlaufer, 2003: The surface physics of ice in thunderstorms. *Can. J. Phys.,* **81,** 201–207, doi:10.1139/p03-011.

——, B. L. Mason, and J. S. Wettlaufer, 2001: Theory of charge and mass transfer in ice–ice collisions. *J. Geophys. Res.,* **106,** 20 395–20 402, doi:10.1029/2001JD900109.

——, A. W. Rempel, and J. S. Wettlaufer, 2006: The physics of premelted ice and its geophysical consequences. *Rev. Mod. Phys.,* **78,** 695–741, doi:10.1103/RevModPhys.78.695.

Deierling, W., W. A. Petersen, J. Latham, S. Ellis, and H. J. Christian, 2008: The relationship between lightning activity and ice fluxes in thunderstorms. *J. Geophys. Res.,* **113,** D15210, doi:10.1029/2007JD009700.

Doviak, R. J., V. N. Bringi, A. Ryzhkov, A. Zahrai, and D. Zrnić, 2000: Considerations for polarimetric upgrades to operational WSR-88D radars. *J. Atmos. Oceanic Technol.,* **17,** 257–278, doi:10.1175/1520-0426(2000)017<0257:CFPUTO>2.0.CO;2.

Dye, J. E., J. J. Jones, A. J. Weinheimer, and W. P. Winn, 1988: Observations within two regions of charge during initial thunderstorm electrification. *Quart. J. Roy. Meteor. Soc.,* **114,** 1271–1290, doi:10.1002/qj.49711448306.

Fisher, R., 1953: Dispersion on a sphere. *Proc. Roy. Soc. London A,* **217,** 295–305, doi:10.1098/rspa.1953.0064.

Hendry, A., and Y. M. M. Antar, 1982: Radar observations of polarization characteristics and lightning-induced realignment of atmospheric ice crystals. *Radio Sci.,* **17,** 1243–1250, doi:10.1029/RS017i005p01243.

Herman, B. M., and L. J. Battan, 1961: Calculations of Mie backscattering from melting ice spheres. *J. Meteor.,* **18,** 468–478, doi:10.1175/1520-0469(1961)018<0468:COMBSF>2.0.CO;2.

Hubbert, J. C., 1994: A comparison of radar, optic, and specular null polarization theories. *IEEE Trans. Geosci. Remote Sens.,* **32,** 658–671, doi:10.1109/36.297983.

——, and V. N. Bringi, 2003: Studies of the polarimetric covariance matrix: Part II: Modeling and polarization errors. *J. Atmos. Oceanic Technol.,* **20,** 1011–1022, doi:10.1175/1456.1.

——, S. M. Ellis, M. Dixon, and G. Meymaris, 2010a: Modeling, error analysis, and evaluation of dual-polarization variables obtained from simultaneous horizontal and vertical polarization transmit radar. Part I: Modeling and antenna errors. *J. Atmos. Oceanic Technol.,* **27,** 1583–1598, doi:10.1175/2010JTECHA1336.1.

——, ——, ——, and ——, 2010b: Modeling, error analysis, and evaluation of dual-polarization variables obtained from simultaneous horizontal and vertical polarization transmit radar. Part II: Experimental data. *J. Atmos. Oceanic Technol.,* **27,** 1599–1607, doi:10.1175/2010JTECHA1337.1.

——, ——, W.-Y. Chang, S. Rutledge, and M. Dixon, 2014: Modeling and interpretation of S-band ice crystal depolarization signatures from data obtained by simultaneously transmitting horizontally and vertically polarized fields. *J. Appl. Meteor. Climatol.,* **53,** 1659–1677, doi:10.1175/JAMC-D-13-0158.1.

Kennedy, P. C., and S. A. Rutledge, 2011: S-band dual-polarization radar observations of winter storms. *J. Appl. Meteor. Climatol.,* **50,** 844–858, doi:10.1175/2010JAMC2558.1.

Krehbiel, P., T. Chen, S. McCrary, W. Rison, G. Gray, and M. Brook, 1996: The use of dual channel circular-polarization radar observations for remotely sensing storm electrification. *Meteor. Atmos. Phys.,* **59,** 65–82, doi:10.1007/BF01032001.

Li, Y., and G. A. Somorjai, 2007: Surface premelting of ice. *J. Phys. Chem.,* **111,** 9631–9637, doi:10.1021/jp071102f.

Libbrecht, K. G., and V. M. Tanusheva, 1998: Electrically induced morphological instabilities in free dendrite growth. *Phys. Rev. Lett.,* **81,** 176–179, doi:10.1103/PhysRevLett.81.176.

——, and ——, 1999: Cloud chambers and crystal growth: Effects of electrically enhanced diffusion on dendrite formation from

neutral molecules. *Phys. Rev. E,* **59,** 3253–3261, doi:10.1103/PhysRevE.59.3253.

——, and H. Yu, 2001: Crystal growth in the presence of surface melting: Supersaturation dependence of the growth of columnar ice crystals. *J. Cryst. Growth,* **222,** 822–831, doi:10.1016/S0022-0248(00)00977-5.

Mardia, K. V., 1972: *Statistics of Directional Data.* Academic Press, 357 pp.

McCormick, G. C., and A. Hendry, 1975: Principles for the radar determination of the polarization properties of precipitation. *Radio Sci.,* **10,** 421–434, doi:10.1029/RS010i004p00421.

Metcalf, J. I., 1995: Radar observations of changing orientations of hydrometeors in thunderstorms. *J. Appl. Meteor.,* **34,** 757–772, doi:10.1175/1520-0450(1995)034<0757:ROOCOO>2.0.CO;2.

Park, S.-G., V. N. Bringi, V. Chandrasekar, M. Maki, and K. Iwanami, 2005: Correction of radar reflectivity and differential reflectivity for rain attenuation at X band. Part I: Theoretical and empirical basis. *J. Atmos. Oceanic Technol.,* **22,** 1621–1632, doi:10.1175/JTECH1803.1.

Petersen, W. A., S. A. Rutledge, and R. E. Orville, 1996: Cloud-to-ground lightning observations from TOGA COARE: Selected results and lightning location algorithms. *Mon. Wea. Rev.,* **124,** 602–620, doi:10.1175/1520-0493(1996)124<0602:CTGLOF>2.0.CO;2.

——, ——, R. C. Cifelli, B. S. Ferrier, and B. F. Smull, 1999: Shipborne dual-Doppler operations during TOGA COARE: Integrated observations of storm kinematics and electrification. *Bull. Amer. Meteor. Soc.,* **80,** 81–97, doi:10.1175/1520-0477(1999)080<0081:SDDODT>2.0.CO;2.

Pruppacher, H. R., and J. D. Klett, 1997: *Microphysics of Clouds and Precipitation.* Kluwer Academic, 954 pp.

Rutledge, S. A., E. R. Williams, and T. D. Keenan, 1992: The Down Under Doppler and Electricity Experiment (DUNDEE): Overview and preliminary results. *Bull. Amer. Meteor. Soc.,* **73,** 3–16, doi:10.1175/1520-0477(1992)073<0003:TDUDAE>2.0.CO;2.

Ryzhkov, A. V., and D. S. Zrnić, 2007: Depolarization in ice crystals and its effect on radar polarimetric measurements. *J. Atmos. Oceanic Technol.,* **24,** 1256–1267, doi:10.1175/JTECH2034.1.

Sazaki, G., S. Zepeda, S. Nakatsubo, M. Yokomine, and Y. Furukawa, 2012: Quasi-liquid layers on ice crystal surfaces are made up of two different phases. *Proc. Natl. Acad. Sci. USA,* **109,** 1052–1055, doi:10.1073/pnas.1116685109.

Seliga, T. A., and V. N. Bringi, 1976: Potential use of radar differential reflectivity measurements at orthogonal polarizations for measuring precipitation. *J. Appl. Meteor.,* **15,** 69–76, doi:10.1175/1520-0450(1976)015<0069:PUORDR>2.0.CO;2.

Vivekanandan, J., G. Zhang, S. M. Ellis, D. Rajopadhyaya, and S. K. Avery, 2003: Radar reflectivity calibration using differential propagation phase measurement. *Radio Sci.,* **38,** 8049, doi:10.1029/2002RS002676.

Wang, Y., and V. Chandrasekar, 2006: Polarization isolation requirements for linear dual-polarization weather radar in simultaneous transmission mode of operation. *IEEE Trans. Geosci. Remote Sens.,* **44,** 2019–2028, doi:10.1109/TGRS.2006.872138.

Williams, E. R., and R. M. Lhermitte, 1983: Radar tests of the precipitation hypothesis for thunderstorm electrification. *J. Geophys. Res.,* **88,** 10 984–10 992, doi:10.1029/JC088iC15p10984.

Workman, E. J., and S. E. Reynolds, 1949: Electrical activity as related to thunderstorm cell growth. *Bull. Amer. Meteor. Soc.,* **30,** 142–144.